Rotor interactional effects on aerodynamic and noise characteristics of a small multirotor unmanned aerial vehicle

Hakjin Lee (이학진)[1, a)] and Duck-Joo Lee (이덕주)[2]

[1]Mechanical Engineering Research Institute, Korea Advanced Institute of Science and Technology (KAIST), 291 Daehak-ro, Yuseong-gu, Daejeon 34141, South Korea

[2]Deparment of Aerospace Engineering, Korea Advanced Institute of Science and Technology (KAIST), 291 Daehak-ro, Yuseong-gu, Daejeon 34141, South Korea

[a)]Author to whom correspondence should be addressed: hakjin@kaist.ac.kr

Abstract

Small scale unmanned aerial vehicles (UAVs) using multirotor propulsion systems have received considerable attention for a wide range of military and commercial applications in recent years. In the multirotor configuration, the rotor interaction phenomenon occurs severely because the rotors are located in close proximity to each other. Therefore, the separation distance between the adjacent rotor tips has a strong effect on the wake structures and flow fields, which consequently play an important role in determining the aerodynamic performance and noise level of the multirotor vehicle. In the present study, numerical simulations of a quadcopter in hover flight conditions are conducted to investigate the mutual rotor-to-rotor interactional effects on the aerodynamic performance, wake structures, and sound pressure level using nonlinear vortex lattice method (NVLM) with vortex particle method (VPM) and acoustic analogy based on Farassat's Formulation 1A. Calculations for the multirotor configurations with different separation distances show that the average thrust force decreases significantly and force fluctuation is found to increase dramatically as the rotor spacing gets smaller. In addition, the wake geometry and induced flow structure behind the rotor tend to be radially dragged down toward the center of the vehicle due to the existence of the adjoining rotor, which consequently results in strong wake-to-wake interaction and the formation of asymmetric wake structures though the multirotor operates in hovering condition. It is also observed that unsteady loading introduced by rotor interaction leads to a considerable increase in the sound pressure level, particularly the normal direction of the rotor plane.

I. INTRODUCTION

Small scale unmanned aerial vehicles (UAVs) based on a multirotor platform, commonly referred to as a drone, have grown to be a useful device for commercial and military applications[1]. The continued growth of multirotor UAVs is closely linked to its simple structure, versatility, maneuverability, affordability, and vertical take-off and landing (VTOL) ability. In particular, the use of the rotor system and VTOL ability provide a viable opportunity to apply the multirotor UAVs for various purposes, such as surveillance, aerial photography, film recording, remote sensing, and also for delivery service[2].

Compared to conventional rotorcraft, small-scale multirotor UAVs have unique aerodynamic features that provide an interesting challenge to the tasks of performance and noise prediction. The modern multirotor UAVs are generally designed for a small-sized configuration so that they can be easily achievable in practice for the various missions. Therefore, they mostly operate under incompressible and low Reynolds number (Re) flow conditions[3-5] where the operating range of Reynolds number is from 10^4 to 10^5. The aerodynamics of an airfoil involved in the rotor blade is affected by the scaling of the Reynolds number, which is defined as the ratio of inertial forces to viscous forces in a fluid. The flow patterns over the airfoil immersed in the fluid are characterized by the Reynolds number[6]. Hence, the rotor blades encounter the considerably different flow speed regime, thus resulting in the notably different aerodynamic behavior of the airfoil in contrast with a full-scale helicopter or rotorcraft operating high Reynolds number flow. When the airfoil encounters the low Reynolds number flow, a slope of lift curve is no longer 2π and lift coefficient tends to nonlinearly change with respect to the angle of attack[7, 8], even before stall (or critical) angle of attack because of nonlinear mechanisms, such as the presence of laminar separation bubble (LSB)[9-14], the occurrences of laminar boundary layer separation[15, 16] and turbulent transition[17, 18]. Hence, the airfoil typically suffers from a notably reduced aerodynamic performance[4, 8, 19-21]. The maximum lift coefficients ($C_{l.max}$) are decreased considerably and drag penalties appear that cause a significant reduction in a lift-to-drag ratio (C_l/C_d) compared to high Reynolds number flow. Therefore, it is imperative to consider the nonlinear aerodynamic behaviors of the airfoil associated with low Reynolds number flow for predicting the vehicles' performance accurately. In the case of the small UAVs, the multirotor systems such as quadcopter or octocopter, are preferable to swashplate mechanisms because they can easily generate the required aerodynamic performance and stabilize the vehicle's attitude through a simple flight control algorithm. However, the rotor-to-rotor interaction phenomenon occurs severely in the multirotor configuration in comparison with the rotary vehicles with a single main rotor. Rotor interactional effects cause highly unsteady and complex flow fields around the neighboring rotors, which is directly related to multirotor UAV's aerodynamic performance, development of wake geometry, vibration, and noise generation. Therefore, for the small scale of multirotor, the range of Reynolds number experienced by the rotor is important, and the rotor interactional effects on its aerodynamics are also significant.

The interactional aerodynamics and acoustics of the multirotor systems have recently been a topic of interest for many researchers. Some experimental studies have been conducted to investigate the aerodynamic and acoustic characteristics of the small multirotor UAVs. Sinibaldi and Marino[22] performed the experimental analysis on the aeroacoustic features of propeller aimed at the propulsion of small multirotor UAVs. Intaratep *et al*.[23] measured both noise and thrust performance of small UAV and studied the effects of multirotor interaction depending on the number of the rotors. Zhou *et al*.[24] conducted an experimental investigation of the impacts of the intervals between the rotors on both the thrust force and noise level of twin-rotor configuration. They also captured the flow fields around the rotors using a high-resolution particle image velocimetry (PIV) system and discussed the complex flow interactions phenomena in detail. Tinney and Sirohi[25] assessed the aerodynamic performance and the near-field acoustics of an isolated rotor, quadcopter, and hexacopter configurations through a six-degree-of-freedom load cell and an azimuthal array of microphones to demonstrate the effects of the number of rotors. Shukla *et al*. experimentally investigated the rotor-rotor[26, 27] and rotor-duct[28] aerodynamic interactional phenomena occurring multirotor systems over a range of hover conditions at low Reynolds number using high-speed stereo PIV and force measurements. The detailed flow structures, wake evolutions, and wake interactions were captured and the interactional aerodynamics were mainly studied. Most of the computational studies used high-fidelity computational fluid dynamics (CFD) tools to numerically investigate the aerodynamic interaction of multirotor flows. Hwang *et al*.[29] conducted unsteady Reynolds-averaged Navier-Stokes (RANS) simulation on the multirotor UAV configuration including four rotors and fuselage under hover and forward flight conditions to examine the mutual aerodynamic interactions between rotor-to-rotor and rotor-to-fuselage. Misiorowski *et al*.[30] also performed a computational study of a quadcopter with different rotor layout for the plus and cross configuration in edgewise flight conditions to study the effects of the rotor interactional aerodynamics on the lift, torque, and pitching moment. Yoon *et al*.[31, 32] investigated the interactional aerodynamics of quad tilt-rotor aircraft under hover flight condition, and discussed the influences of fuselage placement on complex flow physics occurring around small quadcopter vehicle in hover and forward flight conditions using high-fidelity CFD method, i.e. Detached Eddy Simulation (DES). According to the preceding studies[24, 31], a similar consensus on the underlying rotor interactional aerodynamics was reported that individual rotor's performance decreased when the rotors operate in close proximity to each other. More recent numerical studies included the work of Diaz and Yoon[33], which focused on the computational simulation of complete quadcopter configuration including landing gear and a camera in forward flight conditions and sudden wind gusts. Lee *et al.*[34] developed a time-marching free-wake model to analyze the aerodynamic characteristics of the twin-rotor system and studied the wake instability due to wake-wake interaction. In the multirotor systems, the rotor blades encounter the unsteady aerodynamic environment caused by the rotor interaction phenomena, which could also directly affect the sound pressure level radiated from the vehicles. Jia *et al.*[35] and Jia and Lee[36-38] investigated the interactional aerodynamics and acoustics of coaxial rotor and quadrotor eVTOL aircraft using high-fidelity CFD simulations. Ko *et al.*[39] also analyzed the noise directivity patterns depending on the diamond and square formation for the multirotor configuration, as distinct from a single rotor, through the free wake vortex lattice method (VLM). The scattering effects of the quadcopter fuselage with simple monopole acoustic sources on the noise generation and propagation at the near- and far-field were investigated using the boundary element method (BEM)[40].

As mentioned earlier, the mutual interaction between multiple rotors is one of the unique features of the multirotor systems, and it is an important factor to be considered in determining the aerodynamic and aeroacoustic performance of small UAVs because a variation in their performance is not simply proportional to the number of rotors[41]. Although several studies on the multirotor UAVs have been conducted extensively through experiments and the numerical simulations, most of the numerical research has primarily focused on assessing the vehicles' aerodynamic performance rather than predicting the complex wake flow. Besides, the analysis of the interactional acoustics and its effects on the noise characteristics of the multirotor UAVs have not yet been discussed in detail. The rotor interactional phenomena occurring around the multirotor vehicles are significantly influenced by the separation distance defined as a length between the adjacent rotors. The main objective of the present study is to investigate the rotor spacing effects on the interactional aerodynamics and acoustics associated with the multirotor systems. The comprehensive and detailed analysis in terms of the aerodynamic performance, wake structure, flow field, and sound pressure level are performed to achieve a better understanding of the mutual rotor-to-rotor interaction, particularly about noise directivity patterns and the complex wake behavior of multirotor vehicle. In this study, a nonlinear vortex lattice method (NVLM) coupling with a time-accurate vortex particle method (VPM) is used to compute the aerodynamic loads, and describe the unsteady wake flow efficiently. This study addresses the characterization of the aerodynamic performance of small multirotor UAV operating in low Reynolds number flow. NVLM has been suggested to successfully consider the nonlinear aerodynamic characteristics associated with low Reynolds number flow, unlike the widely used conventional VLM. The ability to accurately evaluate the aerodynamic loads acting on the rotor blades can greatly aid in predicting the aeroacoustic features of the multirotor. Farassat's Formulation 1A is utilized for assessing the tonal noise in terms of thickness and loading noise at blade passing frequencies. Before conducting the computational analysis of the multirotor configuration, the numerical methods used in this study are validated against the high-quality measurements on the isolated rotor. Calculations for the multirotor configuration reveals the separation distance between the rotors has a significant effect on the aerodynamic and acoustic characteristics of a quadrotor in hover. Discussion in this study will help to improve our understanding of the underlying interactions in multirotor flows, and it can be used for designing more advanced multirotor vehicles.

II. NUMERICAL METHODS

A. Vortex lattice method

VLM also referred to as a lifting surface method, is one of the most practical approaches for the comprehensive analysis of the rotary systems such as propellers, helicopters and wind turbines. It is capable of accurately calculating the aerodynamic loads on the rotor blades operating incompressible flow with affordable computational costs[42-45]. VLM is based on that the fluid surrounding the body surface and wake regions is assumed to be inviscid, incompressible ($\nabla \cdot \mathbf{V} = 0$) and irrotational ($\nabla \times \mathbf{V} = 0$) flow over the entire domain, and the rotor blade can be regarded as lifting surface without thickness. To solve the lifting surface problem numerically, the camber surface of the rotor blade is divided into quadrilateral singularities containing the constant-strength vortex ring elements ($\Gamma_{i,j}$) that are composed of four concentrated (lumped) vortex filaments with i and j indexing in the chordwise and spanwise directions ($i = 1, \cdots, M$ and $j = 1, \cdots, N$)[46]. The distribution of the vortex ring elements on the camber surface should be satisfied with impermeable boundary condition, also called as zero normal flow boundary condition. The instantaneous zero normal flow boundary condition including time-dependent kinematic velocity term for unsteady rotor simulation can be expressed as in Eqs. (1)–(3).

$$(\nabla\phi + \mathbf{V}) \cdot \mathbf{n} = 0 \tag{1}$$

$$\mathbf{V} = -(\mathbf{V}_0 + \mathbf{\Omega} \times \mathbf{r}) \tag{2}$$

$$(\mathbf{V}_{\text{ind.blade}} + \mathbf{V}_{\text{ind.wake}} + \mathbf{V}_{\infty} - \mathbf{\Omega} \times \mathbf{r}) \cdot \mathbf{n} = 0 \tag{3}$$

Here, ϕ is the velocity potential, $\mathbf{n}$ is the unit normal vector, $\mathbf{V}_{\text{ind.blade}}$ and $\mathbf{V}_{\text{ind.wake}}$ represent the velocity components induced by the bound vortices on the rotor blades and wake vortices, respectively. The kinematic velocity term (**V**) in the body-fixed coordinate is composed of the velocity components due to the translation ($\mathbf{V}_0$) and rotation of the rotor blade ($\mathbf{\Omega} \times \mathbf{r}$) where the translation velocity can be defined in the opposite direction with the freestream velocity ($\mathbf{V}_\infty$).

$$a_{k1}\Gamma_1 + a_{k2}\Gamma_2 + \cdots + a_{kL}\Gamma_L + (\mathbf{V}_{\text{ind.wake}} + \mathbf{V}_\infty - \mathbf{\Omega} \times \mathbf{r})_k \cdot \mathbf{n}_k = 0 \tag{4}$$

$$\begin{bmatrix} a_{11} & a_{12} & \cdots & a_{1L} \\ a_{21} & a_{22} & \cdots & a_{2L} \\ \vdots & \vdots & \ddots & \vdots \\ a_{L1} & a_{L2} & \cdots & a_{LL} \end{bmatrix} \begin{pmatrix} \Gamma_1 \\ \Gamma_2 \\ \vdots \\ \Gamma_s \end{pmatrix} = \begin{pmatrix} \text{RHS}_1 \\ \text{RHS}_2 \\ \vdots \\ \text{RHS}_L \end{pmatrix} \tag{5}$$

$$\text{RHS}_k = -(\mathbf{V}_{\text{ind.wake}} + \mathbf{V}_\infty - \mathbf{\Omega} \times \mathbf{r})_k \cdot \mathbf{n}_k \tag{6}$$

A set of algebraic equations for the unknown strength of bound vortices can be established by applying the instantaneous zero normal flow boundary condition on the collocation point of each vortex element as in Eqs. (4)–(6) where a_{kl} implies the influence coefficient, representing the influence of the l-th vortex ring element at the collocation point of k-th vortex ring element. Here, L is the total number of the vortex ring elements and is defined as $L = M \times N$. Therefore, the sequential index of the vortex ring elements (k, l) has values between 1 and L.

B. Nonlinear vortex lattice method

As aforementioned, low Reynolds number aerodynamics of the airfoils involved in the blade sections has a significant effect on the performance of the small scale multirotor vehicle. However, VLM is intrinsically impossible to consider the nonlinear aerodynamic behavior of airfoil caused by the viscous effect, flow separation, and low Reynolds number flow because it was derived from an assumption of the linear potential flow. In the present paper, NVLM is adopted to compute the aerodynamic loads on the rotor blades, which will be used as the primary input variables for aeroacoustic analysis. NVLM has been suggested to overcome the limitation of existing VLM as mentioned above, and its application to capturing of the nonlinear rotor aerodynamics has been introduced by Lee and Lee[47-50]. The validation results show that NVLM has a great ability to consider the nonlinear aerodynamic characteristics mainly introduced by the viscous effects and low Reynolds number flow through the airfoil look-up table and iterative vortex strength correction.

The sectional flow conditions in terms of the local inflow velocity ($\mathbf{V}_{\text{inflow}}$) and effective angle of attack (α_{eff}) can be computed using Eqs. (7) and (8) after the unknown strength of the bound vortex is determined by solving a linear set of equations derived from VLM.

$$\mathbf{V}_{\text{inflow}} = \mathbf{V}_{\infty} - \mathbf{\Omega} \times \mathbf{r} + \mathbf{V}_{\text{ind.blade}} + \mathbf{V}_{\text{ind.wake}} \tag{7}$$

$$\alpha_{\text{eff}} = \theta_{twist} + \theta_{pitch} + \tan^{-1}\left(\frac{\mathbf{V}_{\text{inflow}} \cdot \mathbf{a}_3}{\mathbf{V}_{\text{inflow}} \cdot \mathbf{a}_1} \right) \tag{8}$$

Here, $\mathbf{a}_1$ and $\mathbf{a}_3$ are the unit tangential and normal vectors to the rotor plane, θ_{twist} and θ_{pitch} are the local twist and blade pitch angles, respectively. Then, the sectional aerodynamic force coefficients, such as thrust (C_T) and torque (C_Q) coefficients, are evaluated using the sectional lift (C_L) and drag (C_D) coefficients obtained from the airfoil look-up table process as a function of the local inflow velocity and effective angle of attack. They are integrated along the span of the rotor blade and multiplied by the number of the blades to compute the overall rotor performance acting perpendicular and tangential to the rotating plane.

The look-up table is a practical and efficient way of considering the nonlinear aerodynamic behaviors of airfoils. The lift, drag and moment coefficients of the airfoil can be obtained through wind tunnel experiments and numerical simulations. Unfortunately, although the airfoil involved in the rotor blades of the small scale multirotor vehicle mostly operates within $10^4 < Re_c < 10^5$ conditions, the wind tunnel measurements for this range of Reynolds numbers are scarce. In the present study, Stanford University Unstructured (SU2) open-source CFD code[51] is used for computing the aerodynamic coefficients of the sectional airfoil as a function of both angle of attack and Reynolds numbers. RANS simulation with the Spalart-Allmaras (S-A) turbulence model with Bas-Cakmakcioglu (B-C) transition model is conducted to capture transitional flow over the airfoil[52]. The B-C transition model is a correlation-based algebraic model, and its underlying turbulence model is the S-A one-equation turbulence model where an algebraic γ-function, rather than the intermittency transport γ-equation, is incorporated into the S-A turbulence model[53].

C. Vortex particle method

The rotor wake originating from the blade is described by the Lagrangian approach, rather than the Eulerian approach. The Lagrangian approaches, such as straight[54] or curved[55, 56] vortex filaments, and vortex particle[57-59] methods, are used a grid-free formulation for wake modeling. Hence, the main advantage of these methods is that the complex wake dynamics occurring around near- and far-fields can be described accurately without the numerical dissipation error introduced by a discretized volume grid. In the present study, NVLM is tightly integrated with a time-accurate vortex particle method (VPM) to simulate the wake flow around the isolated and multirotor configurations. One feature of using VPM is that the wake vortex particles are not required to maintain connectivity between adjacent particles, unlike the vortex filament methods. The vortex particles mutually influence each other and the wake structure consisting of the vortex particles is allowed to be freely deformed and transported downstream. For these reasons, VPM is a useful approach to capture the unsteady wake behaviors occurring due to the rotor-to-wake or wake-to-wake interactional effects.

During the time-marching step for developing wake, the rotor blade is rotating, the blade vortex elements placed on the trailing edge will be shed with local convection velocity and move toward downstream. The nascent wake consisting of the trailed and shed wake vortex filaments is modeled as curved vortex filaments in the early time step, after which they are discretized into the finite number of the vortex particles. For the incompressible potential flow, the convection of individual vortex particles is described by Eq. (9) and their convection velocity ($\mathbf{V}_{\text{conv}}$) is the sum of the freestream velocity and velocity components induced by the bound vortices on the rotor blades and wake vortices as in Eq. (10) where the wake-induced velocity term is composed of the velocity components induced by the curved vortex filaments ($\mathbf{V}_{\text{ind.filament}}$) and vortex particles ($\mathbf{V}_{\text{ind.particle}}$) as in Eq. (11).

$$\frac{d\mathbf{s}_m}{dt} = \mathbf{V}_{\text{conv}}\left(\mathbf{s}_m, t\right) \tag{9}$$

$$\mathbf{V}_{\text{conv}}\left(\mathbf{s}_m, t\right) = \mathbf{V}_\infty + \mathbf{V}_{\text{ind.blade}} + \mathbf{V}_{\text{ind.wake}} \tag{10}$$

$$\mathbf{V}_{\text{ind.wake}} = \mathbf{V}_{\text{ind.filament}} + \mathbf{V}_{\text{ind.particle}} \tag{11}$$

The freestream velocity ($\mathbf{V}_\infty$) and the velocity induced by the vortex elements on the rotor blade ($\mathbf{V}_{\text{ind.blade}}$) and nascent wake panel ($\mathbf{V}_{\text{ind.filament}}$) are computed independently from the VPM. Meanwhile, both the velocity field outside the boundary layer and the velocity induced by the vortex particles ($\mathbf{V}_{\text{ind.particle}}$) are calculated from the convolution of the vorticity field which is represented by a set of p Lagrangian vector-valued particles. The induced velocity at the m-th vortex particle by the vortex particles ($n = 1, 2, \cdots, p$) can be expressed as in Eq. (12).

Here m and n are the vortex particle indices, $\mathbf{s}_m$ is the position vector of the Lagrangian vortex particles, and p is the total number of vortex particles. $\boldsymbol{\alpha}_n$ is the vector-valued total vorticity inside n-th particle. σ_{mn} is a symmetrized smoothing parameter for preventing the singularity problem and ρ is the non-dimensional distance parameter. The relation between the two parameters can be written in Eqs. (13) and (14).

$$\mathbf{V}_{\text{ind.particle}}(\mathbf{s}_m, t) = -\sum_{n=1}^{p} \frac{1}{\sigma_{mn}^3} K(\rho)(\mathbf{s}_m - \mathbf{s}_n) \times \boldsymbol{\alpha}_n \tag{12}$$

$$\sigma_{mn} = \frac{\sqrt{\sigma_m^2 + \sigma_n^2}}{2} \tag{13}$$

$$\rho = \frac{|\mathbf{s}_m - \mathbf{s}_n|}{\sigma_{mn}} \tag{14}$$

where $K(\rho)$ is the regularized kernel for the evaluating the induced velocity, which is formulated using the vorticity distribution function $\xi(\rho)$ and Green's function for the vector stream-function $G(\rho)$ as in Eq. (15). The various forms of the distribution function are available. The three-dimensional high-order algebraic smoothing function proposed by Winckelmans and Leonard[60] is used here and the functions can be expressed as in Eqs. (16) and (17).

$$K(\rho) = \frac{[G(\rho) - \xi(\rho)]}{\rho} \tag{15}$$

$$G(\rho) = \frac{1}{4\pi} \frac{(\rho^2 + 3/2)}{(\rho^2 + 1)^{3/2}} \tag{16}$$

$$\xi(\rho) = -\frac{1}{\rho} \frac{d^2}{d\rho^2} \left(\rho G(\rho)\right) = \frac{15}{8\pi} \frac{1}{(\rho^2 + 1)^{7/2}} \tag{17}$$

To achieve the wake evolution, the convection velocity of the vortex particles is evaluated at each time step and then their locations are determined through a time integration method. 2nd-order Runge-Kutta method is used here. The blades rotate 5 degrees per time step ($\Delta\psi = 5°$) to obtain better flow and acoustic solutions, and the total number of revolution is 20 including 1 revolution for slow starting to prevent wake instability problem. The rotating speed of the rotor blade is increased from zero to the designated speed gradually, and its variation is defined using a sine function.

D. Acoustic analogy

Major sources of the rotor noise can be generally classified into non-deterministic and deterministic components. The former contains the turbulence ingestion noise, blade-wake interaction noise, airfoil-self noise, while the latter includes the thickness noise, loading noise, blade vortex interaction (BVI) noise, and high-speed impulsive (HSI) noise. Among them, thickness and loading noise of the deterministic components are mainly associated with rotating blades, and they have the periodic and tonal noise characteristics, thus leading to high sound pressure level at the rotor blade passage frequency (BPF) and harmonics. Thickness noise occurs due to the flow disturbance excited by the movement of the rotor blades, and loading noise is generated from the pressure fluctuation caused by the aerodynamic loads acting on the blade surface. Our current research is primarily focused on predicting the thickness and loading noise generated by isolated- and multi-rotor configurations, rather than non-deterministic components. BVI and HSI noise are not directly related to the aerodynamic noise of small size UAV propeller operating in hover flight conditions. Although BVI noise is also a part of the loading noise component, it is typically the most intense source of noise when the rotary-wing vehicles operate in descending flight with low-speed[61] and level flight[37, 38] conditions since BVI noise is related to the impulsive loading due to a tip vortex impacting the following blade. Furthermore, HSI noise is mainly associated with the transonic flow and shock phenomena that could occur in the advancing side of the rotating plane. The sound pressure levels of the thickness and loading noise are evaluated through an acoustic analogy using Farassat's Formulation 1A that is a solution for an arbitrary moving surface of the Ffowcs Williams-Hawkings (FW-H) equation with neglecting the quadrupole source term.[62, 63] Farassat's Formulation 1A is an integral method for evaluating aerodynamically generated noise. The thickness and loading noise are modeled with the surface sources in terms of monopole and dipole as in Eqs. (18)–(20) where [] indicates the evaluation of the enclosed quantity a the retarded time (τ) as defined in Eq. (21). τ is the retarded time when the sound is emitted from sources, whereas t is the observer time. Here a_0 is the speed of sound, ρ_0 is the density of air, and r implies the distance between the source ($\mathbf{x}$) and observer ($\mathbf{y}$) positions.

$$p'(\mathbf{x},t) = p'_T(\mathbf{x},t) + p'_L(\mathbf{x},t) \tag{18}$$

$$p'_T(\mathbf{x},t) = \frac{1}{4\pi}\int_{f=0}\left[\frac{\rho_0\left(\dot{v}_n + v_{\dot{n}}\right)}{r\left|1-M_r\right|^2}\right]_{ret} dS + \frac{1}{4\pi}\int_{f=0}\left[\frac{\rho_0 v_n\left(r\dot{M}_r + a_0 M_r - a_0 M^2\right)}{r^2\left|1-M_r\right|^3}\right]_{ret} dS \tag{19}$$

$$p'_L(\mathbf{x},t) = \frac{1}{4\pi a_0}\int_{f=0}\left[\frac{\dot{l}_r}{r\left|1-M_r\right|^2}\right]_{ret} dS + \frac{1}{4\pi}\int_{f=0}\left[\frac{l_r - l_M}{r^2\left|1-M_r\right|^2}\right]_{ret} dS + \frac{1}{4\pi a_0}\int_{f=0}\left[\frac{l_r\left(r\dot{M}_r + a_0 M_r - a_0 M^2\right)}{r^2\left|1-M_r\right|^3}\right]_{ret} dS \tag{20}$$

$$\tau = t - \frac{r}{a_0} = t - \frac{\left|\mathbf{x}-\mathbf{y}\right|}{a_0} \tag{21}$$

$p'_T(\mathbf{x},t)$ and $p'_L(\mathbf{x},t)$ denote the acoustic pressure of the thickness and loading noise, respectively. On the right-hand side of Eqs. (19) and (20), n and r subscript symbols imply the quantities in the normal direction to the blade surface and radiation direction, i.e. v_n is the local velocity of the blade surface in the direction normal to the blade surface, l_r is the component in the radiation direction of the local force that acts on the fluid due to the surface, and M_r is the component of velocity in the radiation direction normalized by the speed of sound.

III. VALIDATION

A. Model and experiment description

The DJI (Da Jiang Innovation) Phantom 2 is the second generation of commercial Phantom RC model developed from the DJI company, and it is one of the most popular commercial UAV models. It has four rotors with connecting arms and a symmetric X-shaped airframe. The rotor of DJI Phantom 2 is composed of the tapered-twisted blades (DJI 9443 model) and their respective chord and twist angle distributions as a function of radial position are depicted in Fig. 1. Geometric information of the DJI 9443 rotor blade can be obtained from the reference,[64] whereas the sectional airfoil profiles are unavailable. Hence, they are extracted by using a digital high-resolution laser scanning. Two-bladed DJI 9443 with a diameter of 0.24 m (9.45 in.) is mounted on the end of the connecting arms and a diagonal length between rotors is 0.35 m. The neighboring rotors are designed to rotate in the opposite direction to balance the angular moment and maintain the rotational attitude of the quadcopter. One set of the rotors rotates in a counterclockwise (CCW) direction, the other rotates in a clockwise (CW) direction when viewed from above. The blade pitch angle is fixed, hence the attitude of the quadcopter is controlled by adjusting the rotational speed of each rotor that is directly connected to an electrically driven motor. In the current study, the rotor speed is changed from 3,000 to 7,200 rpm, which is corresponding to incompressible and low Reynolds number flow as listed in Table 1.

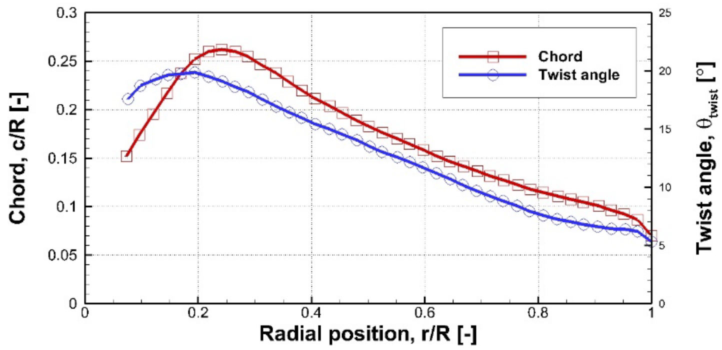

FIG. 1. Chord and twist angle distributions of DJI 9443 rotor blade.

TABLE 1. Geometry information and flow conditions

Parameter	Value
Propeller model	DJI 9443
Number of rotors, N_R [-]	4
Number of blades, N_B [-]	2
Rotor dimeter, D [m]	0.24
Diagonal length, L [m]	0.35
Rotating speed, Ω [rpm]	3,000~7,200
Reynolds number, Re_c [-]	40,000~310,000
Tip Mach number, M_{tip} [-]	0.1~0.26

The multirotor UAVs typically operate under the various flight conditions including hover, vertical (climb and descent) flight, low and high-speed cruises. Among them, they spend considerable time in hover flight conditions to complete their mission. The thrust force and noise level of isolated DJI 9443 rotor blade operating in hover flight were measured for a wide range of rotation rates at structural acoustic loads and transmission (SALT) facility in NASA Langley Research Center where the size of the acoustic facility is 4.57 m (15 ft) high, 7.65 m (25 ft) wide and 9.63 m (31.6 ft) long. Isolated DJI 9443 blade directly mounted the electrically driven motor, and its rotation rate was measured by a laser sensor tachometer. The aerodynamic load and acoustic pressure were recorded under well-controlled conditions by a single-axis load cell and 1/4” Type 4939 free-field

Brüel & Kjaer microphones, respectively. A one-dimensional load cell is placed underneath the motor and a total of five microphones in arc array configuration with an incremental angle of 22.5° degrees are positioned from 45° below the rotating plane to 45° above the rotating plane. A radial distance between the motor hub and microphones is 1.907 m corresponding to approximately $16R$. Here R is the rotor radius. The experimental data are employed to validate the accuracy of the numerical methods used in the present study.

B. Aerodynamic performance

Thrust is the aerodynamic loads applied on the rotor blades in a direction normal to the rotating plane, and it is non-dimensionalized in the form of the thrust coefficient. Figure 2 shows the thrust coefficients comparison between the measurements and calculations for a wide range of operating conditions. NASA experimental data with measurement uncertainty are depicted as a black solid line with circle symbols, and OVERFLOW2 CFD simulation results are described as a magenta dashed line with triangle symbols. The Spalart-Allmaras one-equation turbulence model along with DES and overset grid technique were employed for the viscous and unsteady flow simulation. It is observed that DES simulation yields accurate results compared to the experimental data with the uncertainty associated with the measurements, even though the high-fidelity CFD solutions tend to slightly underestimate the thrust force of the isolated rotor blade in hover. The VLM (blue solid line with diamond symbols) and NVLM (red solid line with square symbols) results are also compared against the experimental data to validate the predictive capability of the numerical models. A discernible difference between VLM and NVLM simulation can be observed clearly, and the significant improvement associated with the considering low Reynolds number effects is easily noticeable as presented in Fig. 2. NVLM results appear to be quite close to the measurements even if the slight discrepancies exist at the rotor speed of 3000 and 7200 rpm, whereas the significant over-prediction in the thrust force coefficient is observed from the VLM simulations owing to the neglecting the nonlinear aerodynamic behaviors of the airfoil associated with low Reynolds number flow. It turns out that the NVLM simulation yields much more accurate results with an average error of 1.3%, whereas the average error of VLM prediction is over 16.2%. Calculations for the isolated rotor under hovering condition show that the present method is capable of accurately computing the aerodynamic loads acting on the rotor blades for small-scale UAV operating low Reynolds number conditions. This will be useful in predicting accurately the aerodynamic noise emitted by the multirotor blades.

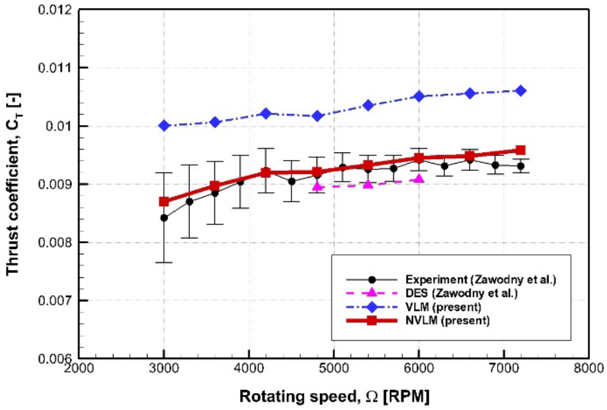

FIG. 2. Comparison of thrust coefficient between the experimental results[64] and numerical predictions.

C. Aerodynamic noise

Acoustic tones associated with rotating blades, which are high sound pressure levels at the BPF and harmonics, are used for comparison between predictions and experiments. As stated previously, thickness and loading noise are mainly considered in this study because they are comparable in amplitude to higher frequency broadband noise. A time series consisting of a sequence of aerodynamic loads acting on the blade surfaces and the geometric information of a rotating blade are used for computing the loading and thickness noise, respectively. After which, the amplitude of acoustic pressure at a given observer position in the time domain is evaluated through Farassat's Formulation 1A. Only time-series data after 15 revolutions, rather than overall time history across all revolutions, are utilized on the acquiring acoustic results in the frequency domain. This post-processing technique can help to more accurately capture the tonal acoustic amplitudes at principal frequencies of interests. The time-series data is processed by using the fast Fourier Transform (FFT) with a Hanning window function to isolate the acoustic contributions of different frequencies. The acoustic spectrum is converted into sound pressure level (SPL) with units of decibels (dB), the resultant overall sound pressure level (OASPL) is then computed by integrating the SPL spectrum.

The experimental acoustic data at five observer positions for the DJI 9443 rotor blade operating at the rotating speeds of 4800, 5400, and 6000 rpm are utilized for validating the aeroacoustic model used in this study. The acoustic performance of the isolated rotor configuration is characterized by the SPL at the specific frequency. Comparing the acoustic tones corresponding to 1st and 2nd BPFs between the measurements and numerical predictions are presented in Figs. 3 and 4, respectively. OF2-PSW implies the predicted noise using a coupled analysis using high-fidelity OVERFLOW2 CFD and PSU-WOPWOP solvers. Figure 3 shows that the predicted

1st BPF noise level at the observer positions appears to be similar and increasing rotation speed is accompanied by increasing pressure amplitude as expected. Furthermore, the 1st BPF noise directivity patterns computed from different simulation techniques, OF2-PSW and NVLM, are well-matched with measurements. (The acoustic data computed from the high-fidelity analysis, denoted as OF2-PSW, are only available at the rotating speed of 5400 rpm) It is worth noting that NVLM predictions are in excellent agreement with measurements within 2 dB, particularly in terms of both acoustic amplitude and directivity behavior. It indicates that the difference in the ability to predict 1st BPF noise directivity is negligible. However, the disparity between the numerical models in the ability to predict the 2nd BPF directivity is observed clearly as shown in Fig. 4. NVLM predictions show reasonable agreement with the measurements, whereas OF2-PSW tends to under-predict the acoustic amplitude of 2nd BPF noise. It turns out that the present method has the capability of accurately predicting the aerodynamically generated tonal noise. However, in the present paper, acoustic analysis is limited to predicting the tonal noise corresponding to 1st and 2nd BPFs. Other higher harmonics at the principal rotor-associated frequencies and broadband noise cannot be captured.

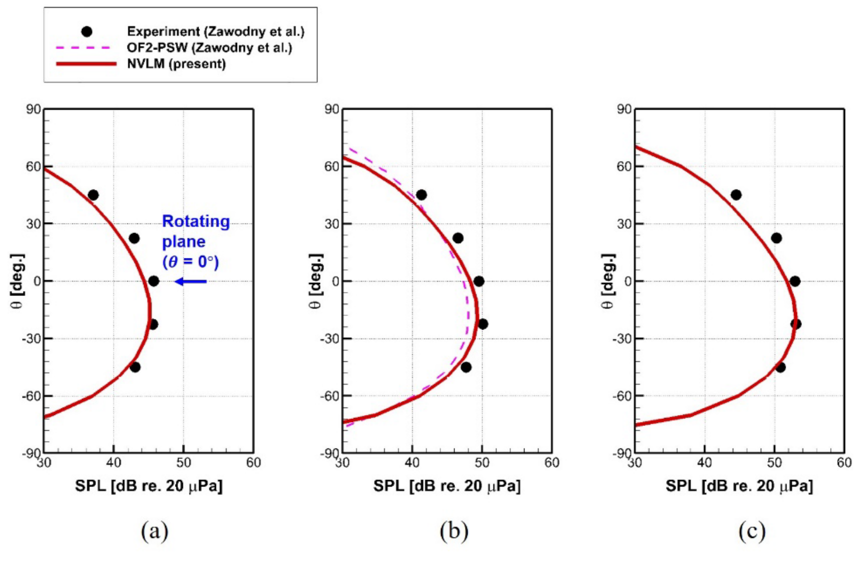

FIG. 3. Comparison of 1st BPF directivity between the experimental results[64] and numerical predictions: (a) Ω = 4800 rpm, (b) 5400 rpm, (c) 6000rpm.

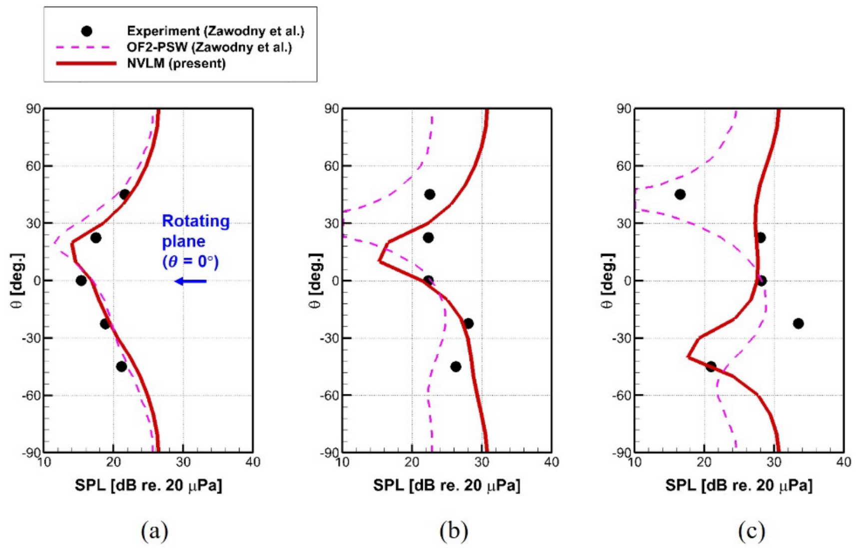

FIG. 4. Comparison of 2nd BPF directivity between the experimental results[64] and numerical predictions: (a) Ω = 4800 rpm, (b) 5400 rpm, (c) 6000rpm.

IV. RESULTS

A. Multirotor configuration

In the present study, numerical simulations of the DJI Phantom 2 quadcopter configuration with the different separation distances are performed to investigate the rotor-to-rotor interactional effects. The separation distance (*d*) is defined as a length between neighboring rotor tips, and it varies from 0.2*D* to 1.0*D* where *D* is the rotor diameter. Only four rotors were considered without connecting arms and fuselage configuration. As depicted in Fig. 5, two of rotors (denoted as rotor 1 and 4) rotate in a counterclockwise (CCW) direction, the others (denoted as rotor 2 and 3) rotate in a clockwise (CW) direction when viewed from above so that trim of the yawing moment is achieved. For the numerical simulation, each rotor blade is modeled by distributing quadrilateral vortex ring elements on the camber surface in the chordwise and spanwise directions. The surface grid resolution of each blade is 30 (chordwise) x 40 (spanwise), and calculations of the quadcopter are carried out at the rotational speed of 5400 rpm. This condition is known as hovering conditions so that the vehicle can remain its flying altitude.

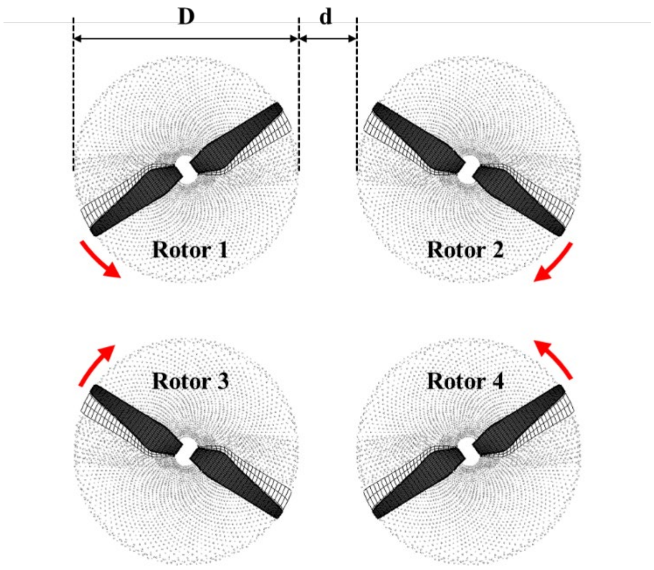

FIG. 5. Multirotor configuration and definition of the separation distance.

B. Thrust force

The influences of the separation distances on the hover performance of quadcopter are examined. Figure 6 shows the comparison of thrust coefficients between the isolated rotor and quadcopter configurations with different separation distances, varying from 0.2*D* to 1.0*D*. Herein, the thrust coefficients of the quadcopter are averaged over one revolution, after which the values of average and standard deviation are divided by the number of the rotors. It can be seen that interactional aerodynamics has exerted a negative influence on the thrust force. The separation distance between the rotors becomes smaller, the average thrust coefficients of quadcopter gradually decrease. Compared to the isolated rotor, the normalized thrust coefficients decrease about 7.93% and 5.91% at the separation distances of 0.2*D* and 0.3*D*, respectively. Similar results were also reported by Zhou *et al.*[4] and Yoon *et al.*[13] who performed the experimental and computational investigations on the aerodynamic interactions of multirotor. When the rotor is positioned at an interval of 0.75*D* away from the neighboring rotors, mutual rotor-to-rotor interaction appears to have little effect on the aerodynamic performance of individual rotors. The average thrust coefficient of quadcopter tends to be close to that of the isolated rotor with increasing separation distance. It is also observed that the separation distance strongly affects the standard deviation of thrust coefficients, as well as average values. When rotors are located close to each other, significant fluctuation in the thrust coefficients occurs as shown in Fig. 7. Calculations for quadcopter configuration with the intervals of 0.2*D* and 0.3*D* show that the thrust coefficients begin to fluctuate dramatically even though the multirotor is operating in hover flight conditions. On the other hand, the thrust fluctuation is gradually alleviated as the separation distance increases, and the oscillation components mostly disappear at the interval of 0.75D and 1.0D where the standard deviation of thrust coefficient decreases to a similar level of that of the isolated rotor. The presence of the severe fluctuation in the thrust coefficients indicates that flow fields around quadcopter and wake flow become highly unsteady. These will be discussed in the following section.

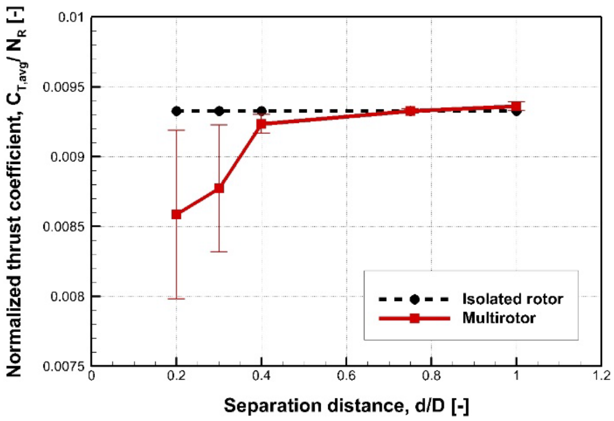

FIG. 6. Normalized thrust coefficient of multirotor depending on the separation distances.

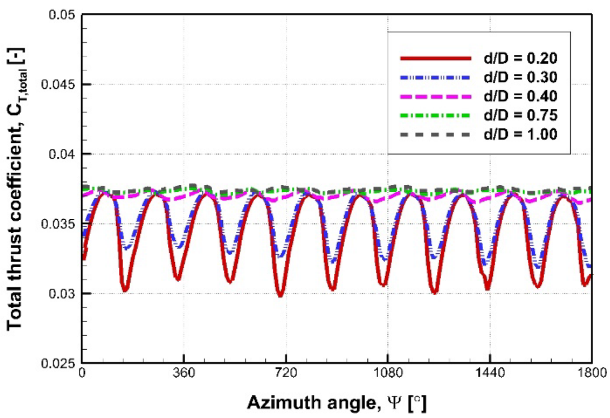

FIG. 7. Time variation in the total thrust coefficient of multirotor depending on the separation distances.

Figure 8 illustrates the radial distributions of an effective angle of attack as a function of the blade azimuth angle that are experienced by the blades of the isolated rotor and multirotor configuration with d = 0.2D, during one rotor revolution. Fig. 8(a) shows that the axially symmetric distribution of the effective angle of attack on the rotor blade is presented in the isolated rotor, but this symmetry is broken in the multirotor as a results of the mutual interference between the rotors. As shown in Fig. 8(b), the unsteady aerodynamic environment of the blade is visible clearly, particularly at the region where $270° < \psi < 360°$ for the rotor 1 and $90° < \psi < 180°$ for the rotor 2. The effective angle of attack at an outboard section of the rotor blade is considerably decreased when each blade of the multirotor passes through this region. Eventually, the rotor blade suffers from the unsteady aerodynamic characteristics during one revolution, which is not observed in the isolated rotor under hover flight.

Figures 9 and 10 show the time variation in the thrust coefficients experienced by the rotor 1 and rotor 2 of multirotor with $d = 0.2D$, respectively. Here, the black dashed line with circle symbols implies the thrust coefficient generated by the isolated rotor, whereas the red solid line without any symbols indicates those generated by the individual rotor of the multirotor. Moreover, the corresponding changes in the thrust coefficients of each blade are described as magenta and blue dashed lines. It should be noted that a marked decline in the thrust force of the multirotor is induced when the rotor blades pass nearby the center of the vehicle where the strong wake interaction is presented because of the upwash that is generated by the wake of adjacent rotors. The direction of this flow is opposite to the direction of wake convection. Upwash flow forces the wake vortices to move from downstream to the upstream, causing the wake recirculation region directly underneath the rotating plane. Wake flow is one of the major factors that contribute to the unsteady aerodynamic behavior of the rotor blade, and it directly causes the inflow velocity on the rotor blade to change with blade azimuth. Then, the rotor blade inevitably suffers from an azimuthal variation in the aerodynamic loads, even though the rotor operates in hover. The unsteady change in the thrust forces acting on each blade is emphasized in the zoomed graph in Figs. 9 and 10, during one revolution. Here, the blade-wake interaction with a periodicity of N-per-revolution can be observed obviously where N is the number of rotor blades. For example, in the case of rotor 1, the blade rotating through the azimuth angle from 270° to 360° encounters highly unsteady inflow caused by the blade-wake interaction, thus leading the significant decrease in the effective angle of attack and resulting thrust force. As might be expected, the neighboring rotors (rotor 1 and rotor 2) have the opposite trends in the change of each blade loading as a function of blade azimuth since they rotate in the opposite direction.

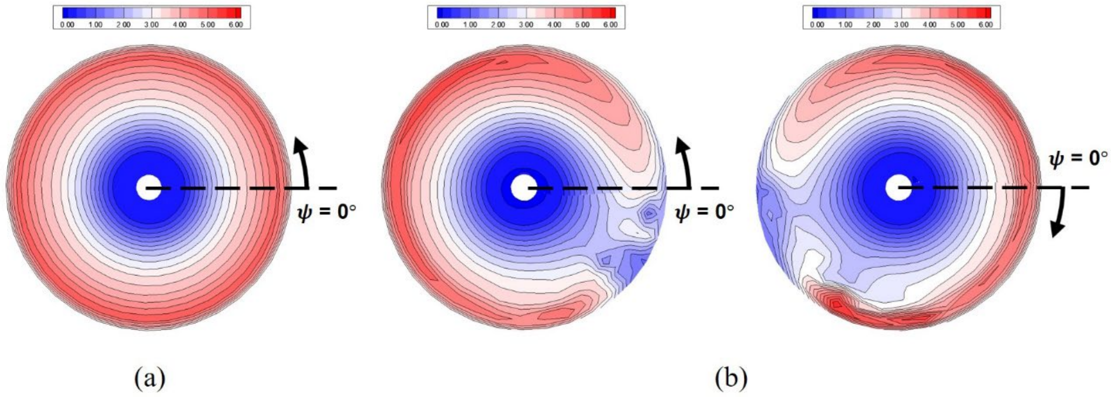

FIG. 8. Comparison of effective angle of attack distribution on the rotor blade: (a) Isolated rotor, (b) Multirotor with $d = 0.2D$ (left: rotor 1, right: rotor 2).

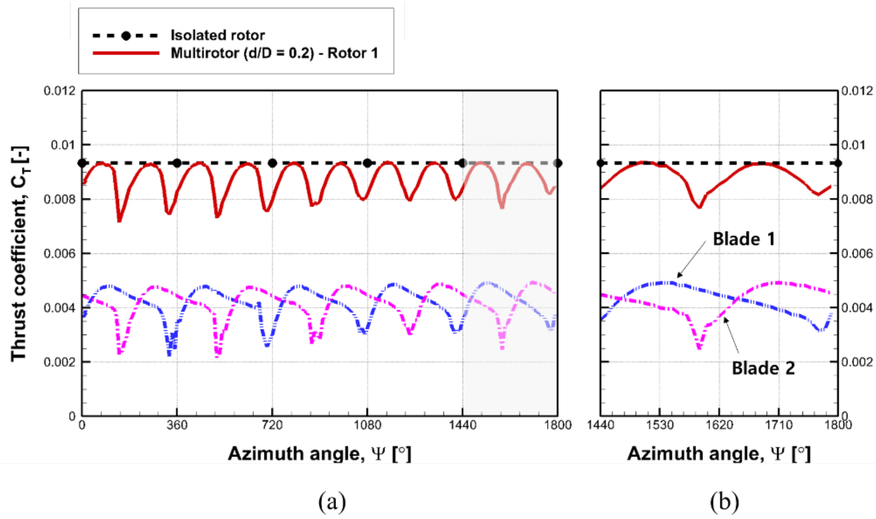

FIG. 9. Time variation in the thrust coefficient experienced by the rotor 1 of multirotor with $d = 0.2D$: (a) during five revolutions, (b) during one revolution.

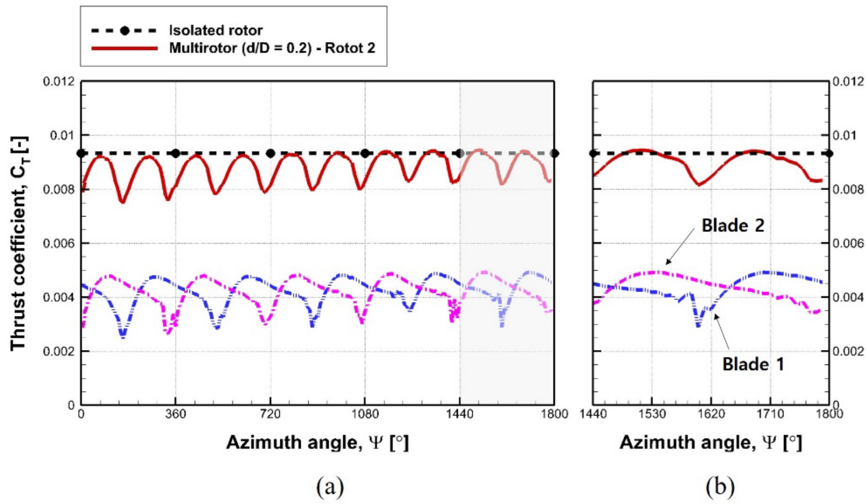

FIG. 10. Time variation in the thrust coefficient experienced by the rotor 2 of multirotor with $d = 0.2D$: (a) during five revolutions, (b) during one revolution.

C. Wake structure

Rotorcraft are most times exposed to the wake flow and its effects. The rotor wake is described to be the unsteady fluctuating flow, which causes the unsteady aerodynamics of the rotor blade and makes the flow field complex. An important attribute of the multirotor configuration as compared to the isolated rotor is the mutual interference between the rotors that directly affects the developing wake geometry. Here, the effects of rotor interaction on the wake evolution of the multirotor operating in hover are discussed.

Figures 11–13 describe varying isolated rotor and multirotor wake geometries with time. As aforementioned, the wake originating from a full span of the rotor blades is represented by Lagrangian based vortex particles. The wake vortex particles are expressed with different sizes depending on the corresponding circulation strength; the stronger the wake vortex strength, the larger the particle size. The color of the vortex particles is also varied with their circulation strength, just as the size does. The developing wake structures of multirotor configurations with the intervals of $0.2D$ and $1.0D$ corresponding to the strongest and weakest interactional effects are compared with those of the isolated rotor. In these sequences of plots, the development of near- and far-wake is well predicted as the rotor revolution is increased. As shown in Fig. 11, the descent of tip vortex and wake contraction can be observed clearly for the isolated rotor. However, for the separation distances of $0.2D$, the wake vortices begin to initially interact with each other as the wake evolves downstream. The individual plots in Fig. 12 show that the inboard edge of the wake vortices tends to attract toward the adjacent rotor, after which the tip vortices merge into a complex vortex structure, particularly at the center of a vehicle. It should also be noted that wake recirculation nearby the rotor blade occurs severely at the 15 revolutions, which is not observed in the isolated rotor operating in hover. As a result, the rotor blade inevitably encounters the wake originating from adjoining rotors in case of the quadcopter with $0.2D$ interval, hence an outboard section of the rotor blade is partially submerged in the wake. These complex wake behaviors occurring around the multirotor are mainly attributed to upwash flow along the opposite direction in the induced velocity. Upwash flow is caused by the wake vortices trailed from the blade tip of adjacent rotors, and it forces the wake vortices to move from the downstream to the upstream. The axial descent rate of the tip vortices is reduced and the wake convection is hampered by their passage through the region where upwash flow is dominant. Therefore, a short length of wake evolution is observed in comparison with that of the isolated rotor case. Reducing the propagation distance and the occurrence of wake recirculation nearby the rotors eventually complicate the flow field and inflow velocity distribution on the blades, which intensify the force fluctuations significantly, as discussed in Fig. 7. However, these features became weakened as the rotor spacing is increased. As might be expected, the wake geometry of the multirotor with $d = 1.0D$ was to be quite similar to that of the isolated rotor case as depicted in Fig 13. It was concluded that when the separation distance becomes larger than $1.0D$, the wake flow seems to have little influence on the wake evolution of the neighboring rotor and the recirculation wake region completely disappears.

(a) (b) (c)

FIG. 11. Wake evolution of the isolated rotor: (a) 5 rev., (b) 10 rev., (c) 15 rev.

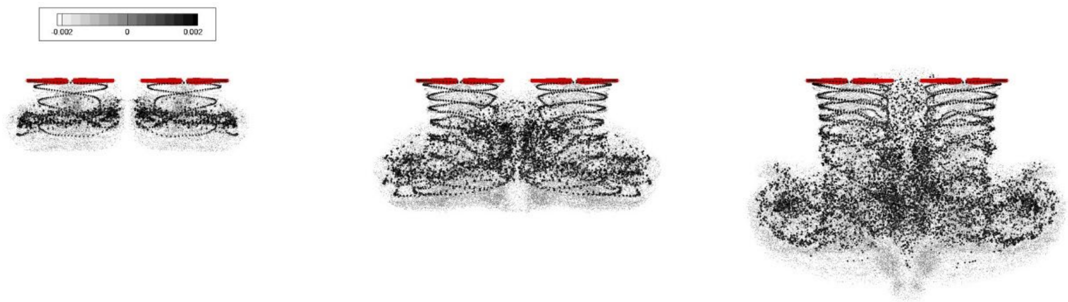

(a) (b) (c)

FIG. 12. Wake evolution of the multirotor with $d = 0.2D$: (a) 5 rev., (b) 10 rev., (c) 15 rev.

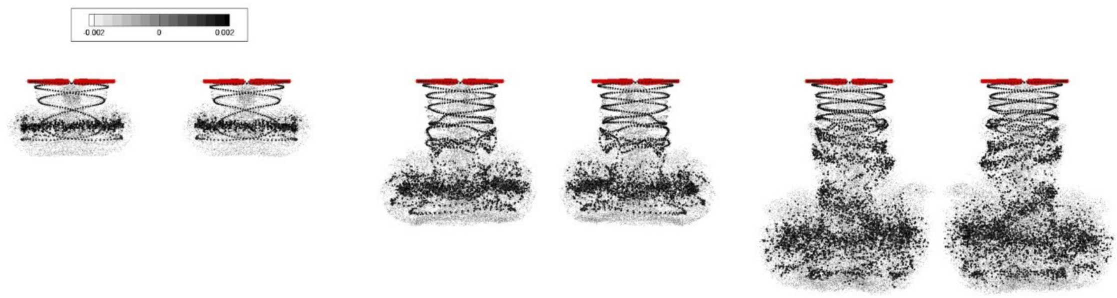

(a) (b) (c)

FIG. 13. Wake evolution of the multirotor with d = 1.0D: (a) 5 rev., (b) 10 rev., (c) 15 rev.

As discussed previously, the wake geometry is strongly influenced by the existence of the tip vortices, which are trailed from the neighboring rotors. Hence, the wake geometries of multirotor UAVs are quite complex. To figure out clearly how the rotor-to-rotor interactions affect the wake geometry, they are decomposed into individual rotor wake and then compared with isolated rotor wake. As shown in Fig. 14, the obvious differences in the wake structures between the two systems are observed as a results of the interactional effects. For the isolated rotor, the near wake is initially developed in a form of helical geometry and it appears to follow a well-defined helical trajectory because rotor interaction is absent, as depicted in Fig. 14(a). Wake structure of the isolated rotor operating in hover propagates axially downstream, and helical tip vortex geometry gradually contracts in a radial direction as wake evolves downstream. During this process, the intermediate wake becomes unstable and highly disordered, eventually its orderly helical structure turns into a distorted form in the further downstream, roughly two rotor diameter below the rotor plane. After which, transition into turbulent wake occurs in the far wake region, and the well-defined helical tip vortex trajectories completely vanish because of their mutual interaction, which is referred to as tip vortex breakdown phenomenon. As shown in Fig. 14(b), although the near wake geometries of the isolated rotor and multirotor with d = 0.2D appear to be similar, the far wake structure is quite different, particularly at the up-right location. The outboard edge of the tip vortices at the right side of the rotor tends to move toward the rotor blade, which is mainly associated with inner upwash flow where the direction of this flow is opposite in the induced velocity. Therefore, asymmetric wake structure rather than orderly helical structure convects downstream and its tip vortex trajectory deviates significantly from a typical rotor wake under hover flight condition. The formation of aperiodic wake structure and upwash flow behind the rotor plane consequently intensify the instability and unsteadiness of the rotor wake. As a result, the overall wake geometry is disrupted at 1.5D, and the tip vortex breakdown accompanying transition into a turbulent wake state occurs much faster than the isolated rotor case. Comparing the wake geometries of the isolated rotor and one rotor of quadcopter shows that the rotor spacing has a strong effect on the wake evolution behind the rotating plane, as well as the aerodynamic performance already studied in Figs. 6 and 7. As expected, the wake structure of the multirotor becomes similar to that of the isolated rotor with increasing the rotor spacing as shown in Fig. 14(c).

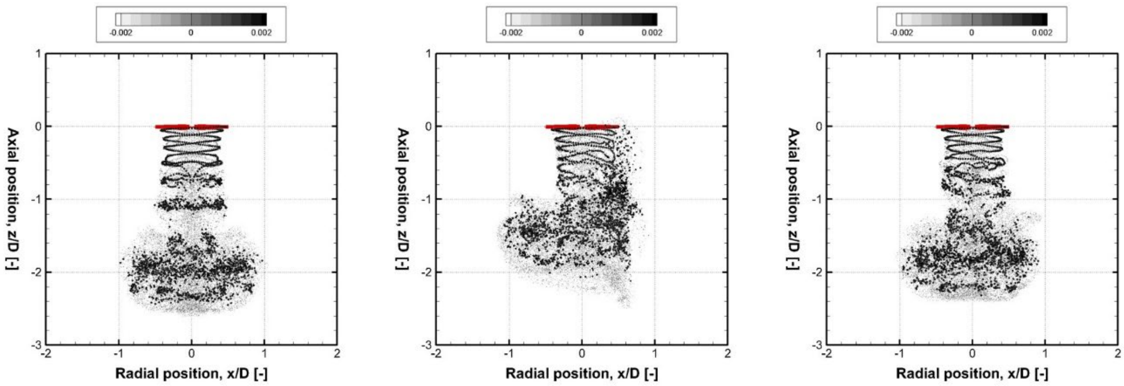

(a) (b) (c)

FIG. 14. Individual rotor wake geometries: (a) Isolated rotor, (b) Multirotor with d = 0.2D, (c) Multirotor with d = 1.0D.

D. Vorticity and flow fields

The vorticity fields are described to further explore the evolution of unsteady wake geometries behind the multirotor along the induced flow direction, which can help to improve our understanding of the rotor interactional effects on the vorticity structure. As shown in Figs. 15 and 16, comparing contours of vorticity magnitude on a vertical cross-section (x-z plane) through the center of the rotating axis shows a notable difference in the vortex structures between the isolated- and multi-rotor where the rotor spacing are 0.2D and 1.0D, respectively. The vorticity contour plots reveal that the periodical shedding of wake vortices behind the rotor plane is well-captured for both cases, which better visualized in Fig. 16. Different color implies the opposite direction of vorticity in the wake vortices. The individual plots in the figure help in identifying the vortex structures, which are mainly composed of tip vortices and shear layers. Pairs of tip vortices are generated due to the pressure difference at the blade tip, while the shear layers are developed by merging of the boundary layers on the upper and lower surfaces of the blade[4]. As expected, the general features of the vorticity distributions around the multirotor with d = 0.2D appear to be quite different from the isolated rotor case, especially at the center of the vehicle where the wake vortices interact severely with each other. The vortex structure of the isolated rotor was found to be developed symmetrically, while that of multirotor with the separation distance of 0.2D tends to shift radially downward to the neighboring rotor, which is believed to be the resultant effect of rotor interaction. These are consistent with the predicted results in Fig. 14, depicting unsteady behavior of wake geometries. In addition, coherent vortical structures are formed in the near wake region, but soon after, they are completely disrupted due to the existence of the consecutive tip vortices trailed from the adjacent rotors. The inner vortex structures including tip vortices and shear layers eventually coalesce into highly disordered vortex structures in the far wake region. It can be also observed that the tip vortices placed on the outboard of individual rotor tend to extensively roll about each other where the direction of wake roll-up is same as the direction of vorticity in the tip vortices trailed from each rotor, which is not observed for the isolated rotor and multirotor with d = 1.0D cases.

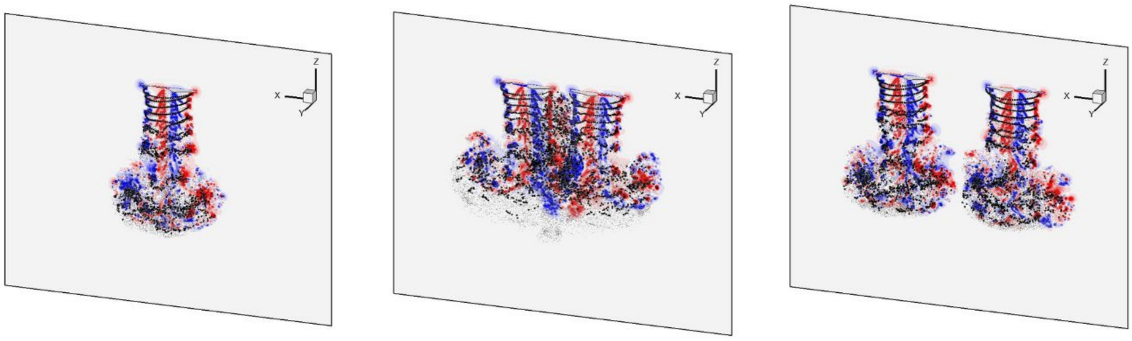

(a) (b) (c)

FIG. 15. Wake structures and vorticity contour on the vertical (x-z) and horizontal (x-y) planes: (a) Isolated rotor, (b) Multirotor with d = 0.2D, (c) Multirotor with d = 1.0D.

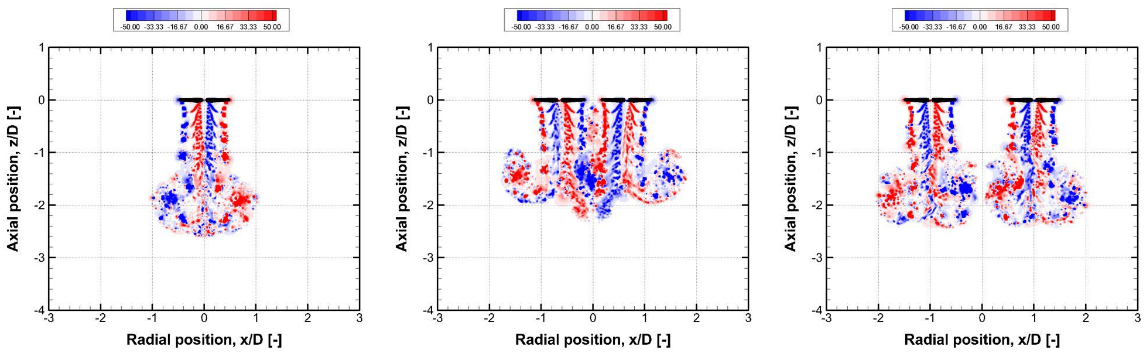

(a) (b) (c)

FIG. 16. Comparison of vorticity contour on the vertical plane (y = 0): (a) Isolated rotor, (b) Multirotor with d = 0.2D, (c) Multirotor with d = 1.0D.

Velocity contours are useful in identifying the flow field that directly affects the rotor performance. The instantaneous axial velocity along the induced flow direction presented here can be used to understand how the rotor-to-rotor interactions affect the flow structures behind the isolated rotor and multirotor. Figures 17 and 18 show the corresponding velocity field, where the induced flow on the rotor blade and unsteady wake flow behind the rotor are well-captured. Each figure contains the plots of axial velocity contour on the vertical (x-z plane) and horizontal (x-y plane) cross-sections where the velocity data are extracted at the center of the rotor and a distance of $1.0D$ form the rotating plane. The velocity contours behind the isolated rotor were found to be axially symmetric and circular, and the significant axial convection and radial contraction of the wake flow are evident as depicted in Figs. 17(a) and 18(a). However, carefully inspecting the flow structures behind the multirotor with the rotor spacing of $0.2D$ in Figs. 17(b) and 18(b), two differences can be identified as distinct from the isolated rotor. The first difference is the existence of strong upwash flow at the center of the vehicle, which is better visualized in Fig. 18(b) where the region occurring upwash flow (positive vertical velocity) can be observed clearly. The direction of upwash flow is the opposite direction in the induced velocity, moving from the downstream to upstream (along positive z-direction in this study). Upwash flow is the most prominent feature of the rotor-to-rotor interaction that is closely pertaining to the periodical shedding of tip vortices trailed from the adjoining rotors. Within the near wake region, upwash flow could interact with the radial flow of the rotor blade that leads to unsteady rotor aerodynamics such as flow separation. In addition, upwash flow between and just below the rotors makes the wake structures complex, forming aperiodic tip vortex trajectory. This observation is already discussed in Figs. 12 and 14, indicating the different axial convection rate of the tip vortices generated from the individual rotor of the multirotor as a results of the existence of upwash flow. This flow not only intensifies the wake interaction severely but also accompanies the low-pressure region at the center of the vehicle. The low-pressure region causes the flow structures to move radially toward the nearby rotors, as shown clearly in Fig. 17(b). This phenomenon is the second difference between the multirotor with $d = 0.2D$ and the rest of the configurations. It is observed that the flow structures behind the rotor tend to be radially dragged down toward the adjoining rotor when the rotors are located near each other, which could be explained by the Coanda effect[4]. This phenomenon is consistent with a bending of the wake geometry of individual rotor as shown in Figs. 12 and 14. The wake structure and induced flow field behind each rotor were found to bend toward the center of the vehicle because of the existence of the low-pressure region and strong interactional effect. A reflected flow structure in the radial direction implies that the rate of change of axial momentum on each rotor is reduced, thus consequently leading to a decrease in the resultant axial force (i.e. thrust force). As revealed clearly in Fig. 18(c), upwash flow becomes less pronounced with increasing the separation distance, the axial velocity distribution around the individual rotor of multirotor with the interval of 1.0D appears to be similar with that of the isolated rotor.

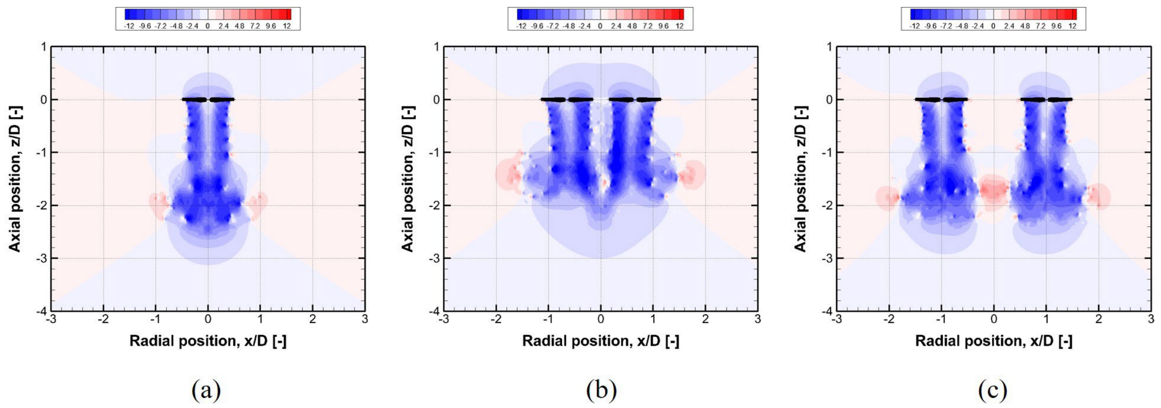

FIG. 17. Comparison of axial velocity contour on the vertical plane (y = 0): (a) Isolated rotor, (b) Multirotor with d = 0.2D, (c) Multirotor with d = 1.0D.

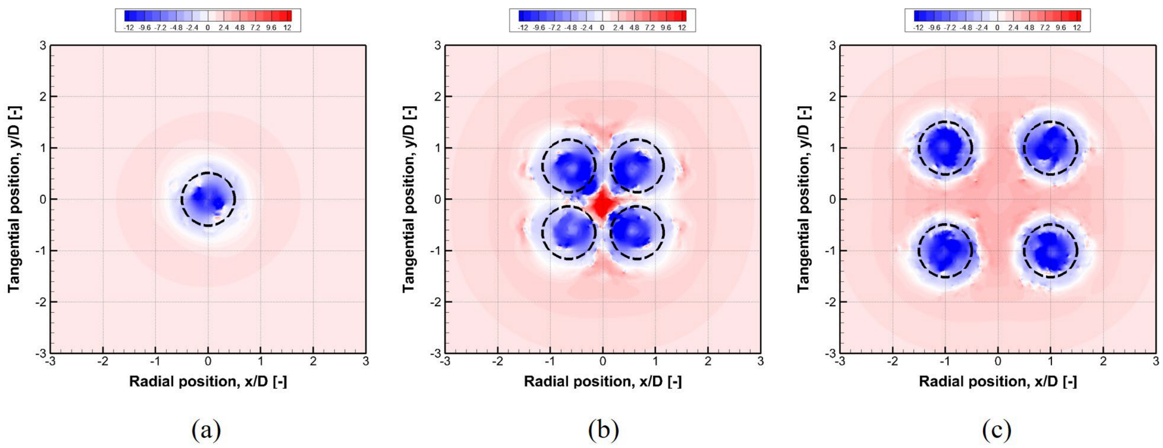

FIG. 18. Comparison of axial velocity contour on the horizontal plane (z = 1.0D): (a) Isolated rotor, (b) Multirotor with d = 0.2D, (c) Multirotor with d = 1.0D.

E. Noise directivity

Two acoustic metrics, including the overall sound pressure level (OASAL) and time-dependent acoustic pressure signal at the observer points, are used in this study for investigating the rotor interactional effects on the noise characteristics of the multirotor. As mentioned previously, the tonal noise components at principal rotor-associated frequencies, namely harmonics of the BPF, generated by the passage of air over the blade of multirotor are predicted using NVLM and acoustic analogy. The observers for computing noise amplitude are located above and below the plane of the rotor, including -180° < θ < 180°, where θ is the observe azimuth angle, and they are positioned at a radial distance of approximately $16R$ from the center of the vehicle.

Figure 19 presents the OASPL directivities as a function of the observer azimuth angle of multirotor configuration with different separation distances. It indicates that the dipole directivity patterns mainly associated with loading noise are observed because the aerodynamic loads acting on the rotor blade are typically the most dominant noise source rather than a thickness nose. The directivity behavior was found to be similar for both cases. However, it can be reasonably expected that the resulting OASPL acoustic amplitudes of multirotor with $d = 0.2D$ much higher than those of the multirotor with $d = 1.0D$ because small rotor spacing intensifies the force fluctuation significantly. As discussed previously, a considerable thrust fluctuation occurs, even if the multirotor operates in hover flight conditions as the separation distance between the rotor becomes smaller. Hence, the unsteady aerodynamic loading introduced by severe rotor interaction causes an increase in the sound pressure level, especially the normal direction of the rotor plane (θ = 90°). On the other hand, the slight difference in noise amplitude between the two multirotor configurations is exhibited by the observers located at the in-plane (θ = 0°) since thickness noise is the main noise contributor in the perpendicular direction of the rotating axis. These results can be also explained by the acoustic pressure signals in the time domain with respect to the observer positions, as shown in Fig. 20. The individual plots present comparing time histories of acoustic pressure as a function of observer time between two multirotor configurations. Figure 20 shows the periodic behavior related to the rotor revolution for all observer positions. However, it is noticeable that the amplitude of time-dependent acoustic pressure of the multirotor with $d/D = 0.2$ is much higher than that of the multirotor with $d/D = 1.0$ except for in-plane location. This informative observation implies that unsteady loading noise caused by strong rotor interaction is the primary acoustic contributor to the multirotor system, being responsible for a significant increase in the amplitude of acoustic pressure with peak pressure events, particularly at observer position of θ = 45° and 90°. It turns out that the rotor interaction strongly affects the noise characteristics of the multirotor operating in hover as well as the aerodynamic performance.

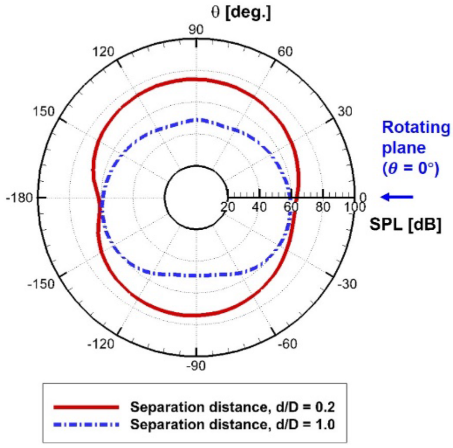

FIG. 19. Comparison of OASPL directivity of multirotor depending on separation distances.

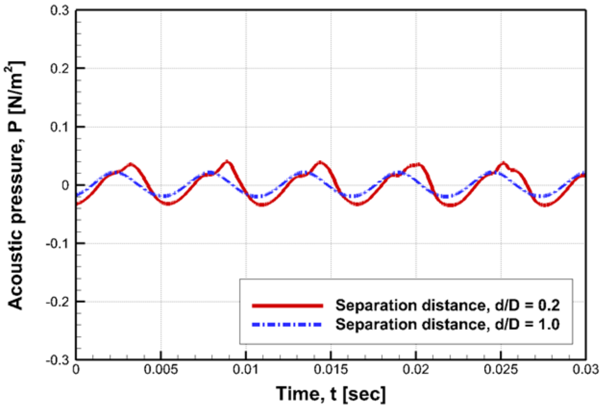

(a)

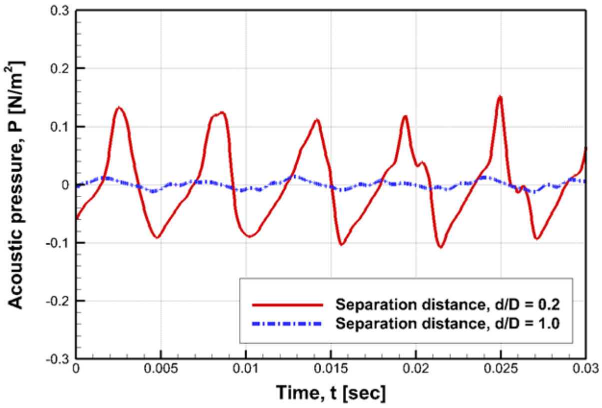

(b)

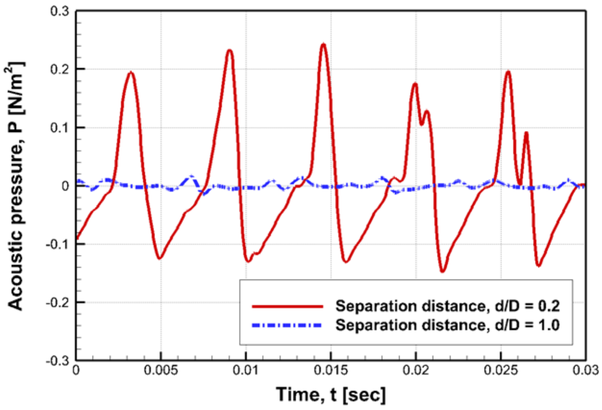

(c)

FIG. 20. Comparison of time-dependent acoustic pressure at the observer positions: (a) θ = 0°, (b) 45°, (c) 90°.

V. CONCLUSION

A comprehensive and versatile analysis of the aerodynamic and aeroacoustic responses of a small-sized multirotor UAVs was presented in this paper. The main focus of the present study was to investigate the influences of the spacing between rotor tips on the thrust force, wake geometry, flow field, and acoustic characteristics of a small-scale multirotor UAV. In the present study, NVLM coupling with VPM and acoustic analogy were adopted for assessing the aerodynamic performance and noise level, respectively. Prediction of noise radiated from rotor blades of isolated- and multi-rotor configurations has been primarily focused on the deterministic aerodynamic noise components, including thickness and loading noise. Our findings in this study are summarized as follows:

1. The rotor interactional effects manifest clearly as decreasing the separation distance for the multirotor configuration.
2. Within the interaction region, particularly at the center of the vehicle and just behind the rotor plane, the tip vortices trailed from the rotor blade generate a strong upwash flow in the opposite direction of induced velocity. Upwash flow impedes the wake convection toward downstream and intensifies wake interactions. Therefore, the aperiodic wake structure rather than orderly helical form is developed althrough the multirotor operates in hover, thus resulting in faster destruction of helical tip vortex trajectory and transition into turbulent wake compared to the isolated rotor case.
3. The occurrence of upwash flow is one of the main features of the severe rotor interaction, which causes not only the formation of asymmetric wake geometry but also the low-pressure region between the rotors. Then, the induced wake flow fields behind each rotor tend to radially bend toward the adjacent rotor, as distinct from the isolated rotor.
4. The mutual rotor interaction complicates the wake flow field, which makes the inflow velocity on the rotor blade highly unsteady. For the multirotor under hovering condition, the rotor blades eventually suffer from the time-variant aerodynamic loads with respect to the rotor azimuth angle, thus leading to a decrease in average hover performance.
5. Finally, the rotor interaction phenomenon not only adversely affects rotor performance but also significantly increases the sound pressure level related to unsteady loading noise, especially the normal direction of the rotor plane. Increasing rotor spacing is an efficient way of alleviating the rotor interactional effects for the multirotor, consequently helps to relieve the force fluctuation and increased noise level as well.

Knowledge of the flow features introduced by the interactional aerodynamics and acoustics is required to optimize the multirotor platform for better design of next-generation UAVs. The present paper is a first step to uncover the dominant flow physics occurring around the multirotor systems. Discussion in this study can help to understand the underlying rotor-to-rotor interaction phenomena and gives scope for further research on noise reductions of multirotor UAVs by controlling rotor spacing.

In general, the multirotor UAVs are equipped with many kinds of devices, such as cameras, sensors, packages, depending on their purpose of use. Rotor wake flow with highly fluctuating velocity components could intensify the fatigue loads of the fuselage, connecting arm, and equipment. A limitation of the present study is that fuselage and connecting arm configurations have not been considered, hence the rotor-airframe interaction effects on aerodynamics and noise generation were not included. Besides, models for assessing the broadband noise are also needed to consider the contribution of the non-deterministic noise components. The rotor-fuselage interactional effects and predicting broadband noise will be discussed in our future study.

ACKNOWLEDGMENTS

This research was conducted at High-Speed Compound Unmanned Rotorcraft (HCUR) research laboratory with the support of Agency for Defense Development (ADD).

[1] G. Cai, J. Dias, and L. Seneviratne, “A Survey of Small-Scale Unmanned Aerial Vehicles: Recent Advances and Future Development Trends,” Unmanned Systems **2**(2) 175–199 (2014).

[2] H. Shakhatreh, A. H. Sawalmeh, A. Al-Fuqaha, Z. Dou, E. Almaita, I. Khalil, N. S. Othman, A. Khreishah, M. Guizani, "Unmanned Aerial Vehicles (UAVs): A Survey on Civil Applications and Key Research Challenges," IEEE Access **7**, 48572–48634 (2019).

[3] P. B. S. Lissaman, “Low-Reynolds-number airfoils,” Annu. Rev. Fluid Mech. **15**, 223–239 (1983).

[4] T. J. Mueller and J. D. DeLaurier, “Aerodynamics of small vehicles,” Annu. Rev. Fluid Mech. **35**, 89–111 (2003).

[5] L. A. Young, “Conceptual Design Aspects of Three General Sub-Classes of Multi-Rotor Configurations: Distributed, Modular, and Heterogeneous,” in *The 6th AHS Specialists Meeting on Unmanned Rotorcraft Systems*, 2015.

[6] D. J. Pines and F. Bohorquez, “Challenges Facing Future Micro-Air-Vehicle Development,” J. Aircraft **43**(2), 290–305 (2006).

[7] A. Pelletier, and T. J. Mueller, “Low Reynolds Number Aerodynamics of Low-Aspect-Ratio, Thin/Flat/Cambered-Plate Wings,” J. Aircraft **37**(5), 825–832 (2000).

[8] S. Wang, Y. Zhou, Md. Mahbub Alam, and H. Yang, "Turbulent intensity and Reynolds number effects on an airfoil at low Reynolds numbers," Phys. Fluids **26**, 115107 (2014).

[9] M. M. O'Meara, and T. J. Mueller, "Laminar Separation Bubble Characteristics on an Airfoil at Low Reynolds Number," AIAA J. 25(8), 1033–1041 (1987).

[10] L. E. Jones, R. D. Sandberg, and N. D. Sandham, "Direct numerical simulations of forced and unforced separation bubbles on an airfoil at incidence," J. Fluid Mech. **602**, 175–207 (2008).

[11] L. E. Jones, R. D. Sandberg, and N. D. Sandham, "Stability and receptivity characteristics of a laminar separation bubbleon an aerofoil," J. Fluid Mech. **648**, 257–296 (2010).

[12] A Crivellini1, V. D'Alessandro, D. Di Benedetto, S. Montelpare and R. Ricci, "Study of laminar separation bubble on low Reynolds number operating airfoils: RANS modelling by means of an high-accuracy solver and experimental verification," J. Phys.: Conf. Ser. **501**, 012024 (2014).

[13] D. Lee, S. Kawai, T. Nonomura, M. Anyoji, H. Aono, A. Oyama, K. Asai, and K. Fujii, "Mechanisms of surface pressure distribution within a laminar separation bubble at different Reynolds numbers," Phys. Fluids **27**, 023602 (2015).

[14] D. Park, H. Sim, and Y. Lee, "PIV Measurement of Separation Bubble on an Airfoil at Low Reynolds Numbers," J. Aerosp. Eng. **33**(1), 04019105 (2020).

[15] T. J. Mueller, and S. M. Batill, "Experimental Studies of Separation on a Two-Dimensional Airfoil at Low Reynolds Numbers, AIAA J. **20**(4), 457–463 (1982).

[16] J. C. M. Lin, and L. L. Pauley, "Low-Reynolds-Number Separation on an Airfoil," AIAA J. **34**(8), 1570–1577 (1996).

[17] M. S. H. Boutilier, and S. Yarusevych, "Separated shear layer transition over an airfoil at a low Reynolds number," Phys. Fluids **24**, 084105 (2012).

[18] H. Dong, T. Xia, L. Chen, S. Liu, Y. D. Cui, B. C. Khoo, and A. Zhao, "Study on flow separation and transition of the airfoil in low Reynolds number," Phys. Fluids **31**, 103601 (2019).

[19] H. Shan, L. Jiang, and C. Liu, "Direct numerical simulation of flow separation around a NACA0012 airfoil," Comput. Fluids **34**, 1096–1114 (2005).

[20] R. Kojima, T. Nonomura, A. Oyama, and K. Fujii, "Large-eddy simulation of low-Reynolds-number flow over thick and thin NACA airfoils," J. Aircraft **50**(1), 187-196 (2013).

[21] M. Anyoji, T. Nonomura, H. Aono, A. Oyama, K. Fujii, H. Nagai and K. Asai, "Computational and Experimental Analysis of a High-Performance Airfoil Under Low-Reynolds-Number Flow Condition," J. Aircraft **51**(6), 1864–1872 (2014).

[22] G. Sinibaldi, and L. Marino "Experimental analysis on the noise of propellers for small UAV," Appl. Acoustics **74**(1), 79-88 (2013).

[23] N. Intaratep, W. N. Alexander, W. J. Devenport, S. M. Grace, and A. Dropkin, "Experimental Study of Quadcopter Acoustics and Performance at Static Thrust Conditions," AIAA Paper No. 2016-2873, 2016.

[24] W. Zhou, Z. Ning, H. Li, and H. Hu, "An Experimental Investigation on Rotor-to-Rotor Interactions of Small UAV," AIAA Paper No. 2017-3744, 2017

[25] C. E. Tinney, and J. Sirohi, "Multirotor Drone Noise at Static Thrust," AIAA J. **56**(7), 2816-2826 (2018).

[26] D. Shukla, and N. Komerath, "Multirotor Drone Aerodynamic Interaction Investigation," Drones **2**(4), 43 (2018).

[27] D. Shukla, and N. Komerath, "Drone Scale Coaxial Rotor Aerodynamic Interactions Investigation," J. Fluids Eng. **141**(7)**,** 071106 (2019).

[28] D. Shukla, and N. Komerath, "Rotor-duct aerodynamic and acoustic interactions at low Reynolds number," Exp. Fluids **60,** 20 (2019).

[29] J. Y. Hwang, M. K. Jung, and O. J. Kwon, "Numerical Study of Aerodynamic Performance of a Multirotor Unmanned-Aerial-Vehicle Configuration," J. Aircraft **52**(3), 839-846 (2015).

[30] M. Misiorowski, F. Gandhi, and A. A. Oberai, "Computational Study on Rotor Interactional Effects for a Quadcopter in Edgewise Flight," AIAA J. **57**(12), 5309-5319 (2019).

[31] S. Yoon, H. C. Lee, and T. H. Pulliam, "Computational Analysis of Multi-Rotor Flows," AIAA Paper No. 2016-0812, 2016.

[32] S. Yoon, P. V. Diaz, D. D. Boyd Jr, W. M. Chan, and C. R. Theodore, "Computational Aerodynamic Modeling of Small Quadcopter Vehicles," in *American Helicopter Society (AHS) 73th Annual Forum & Technology Display*, 2017.

[33] P. V. Diaz, and S. Yoon, "High-Fidelity Computational Aerodynamics of Multi-Rotor Unmanned Aerial Vehicles," AIAA Paper No. 2018-1266, 2018.

[34] J. Lee, K. Yee, and S. Oh, "Aerodynamic Characteristic Analysis of Multi-Rotors Using a Modified Free-Wake Method," Trans. Japan Soc. Aero. Space Sci. **52**(177), 168-179 (2009).

[35] Z. Jia, S. Lee, K. Sharma and K.S. Brentner, "Aeroacoustic Analysis of a Lift-Offset Coaxial Rotor Using High-Fidelity CFD/CSD Loose Coupling Simulation," J. Am. Helicopter Soc. **65**(1), 012011 (2020).

[36] Z. Jia and S. Lee, "Impulsive Loading Noise of a Lift-Offset Coaxial Rotor in High-Speed Forward Flight," AIAA J. **58**(2), 687-701 (2020).

[37] Z. Jia and S. Lee, "Acoustic Analysis of Urban Air Mobility Quadrotor Aircraft," in *Vertical Flight Society (VFS) Aeromechanics for Advanced Vertical Flight Technical Meeting*, 2020

[38] Z. Jia and S. Lee, "Acoustic Analysis of a Quadrotor eVTOL Design via High-Fidelity Simulations," AIAA Paper No. 2019-2631, 2019.

[39] J. Ko, J. Kim, and S. Lee, "Computational Study of Wake Interaction and Aeroacoustic Characteristics in Multirotor Configurations," in *INTER-NOISE 2019*, 2019.

[40] H. Jiang, T. Zhou, R. Fattah, X. Zhang, and X. Hung, "Multi-rotor noise scattering by a drone fuselage," AIAA Paper No. 2019-2586, 2019.

[41] S. Yoon, H. C. Lee, and T.H. Pulliam, "Computational Study of Flow Interactions in Coaxial Rotors," in *AHS Technical Meeting on Aeromechanics Design for Vertical Lift*, 2016.

[42] J. G. Leishman, M. J. Bhagwat, and A. Bagai, "Free-Vortex Filament Methods for the Analysis of Helicopter Rotor Wakes," J. Aircraft **39**(5), 759-775 (2002).

[43] H. Yeo, and W. Johnson, "Assessment of Comprehensive Analysis Calculation of Airloads on Helicopter Rotors," J. Aircraft **42**(5), 1218-1228 (2005).

[44] K. M. Kecskemety, and J. J. McNamara, "Influence of Wake Effects and Inflow Turbulence on Wind Turbine Loads," AIAA J. **49**(11), 2564-2576 (2011).

[45] K. Boorsma, M. Hartvelt, and L. M. Orsi, "Application of the lifting line vortex wake method to dynamic load case simulations," J. Phys.: Conf. Ser. **753**(2), 022030 (2016).

[46] J. Katz, and A. Plotkin, "Low-Speed Aerodynamics," Cambridge University Press, 32 Avenue of the Americas, New York, NY 10013-2473, USA (2012).

[47] H. Lee, and D. J. Lee, "Numerical investigation of the aerodynamics and wake structures of horizontal axis wind turbines by using nonlinear vortex lattice method," Renew. Energy **132**, 1121-1133 (2019).

[48] H. Lee, and D. J. Lee, "Wake impact on aerodynamic characteristics of horizontal axis wind turbine under yawed flow conditions," Renew. Energy **136**, 383-392 (2019).

[49] H. Lee, and D. J. Lee, "Effects of platform motions on aerodynamic performance and unsteady wake evolution of a floating offshore wind turbine," Renew. Energy **143,** 9-23 (2019).

[50] H. Lee, and D. J. Lee, "Low Reynolds number effects on aerodynamic loads of a small scale wind turbine," Renew. Energy, in Press. (2020).

[51] T. D. Economon, F. Palacios, S. R. Copeland, T. W. Lukaczyk, and J. J. Alonso, "SU2: An Open-Source Suite for Multiphysics Simulation and Design," AIAA J. **54**(3)**,** 828-846 (2016).

[52] Y. Jo, T. Jardin, R. Gojon, M. C. Jacob, and J. M. Moschetta, "Prediction of Noise from Low Reynolds Number Rotors with Different Number of Blades using a Non-Linear Vortex Lattice Method," AIAA Paper No. 2019-2615, 2019.

[53] S. C. Cakmakcioglu, O. Bas, and U. Kaynak, "A correlation-based algebraic transition model," Proc IMechE Part C: J Mechanical Engineering Science **232**(21)**,** 3915-3929 (2018).

[54] D. R. Clark, and A. C. Leiper, "The Free Wake Analysis," J. Am. Helicopter Soc. **15**(1), 3-11 (1970).

[55] K. H. Chung, C. J. Hwang, D. J. Lee, and J. B. Yim "Numerical Investigation on a Rotor Tip-Vortex Instability in Very Low Advance Ratio Flight," Int. J. Aeronaut. Space Sci. **6**(2)**,** 84-96 (2005).

[56] D. B. Bliss, and W. O. Miller, "Efficient Free Wake Calculations Using Analytical/Numerical Matching," Am. Helicopter Soc. **38,** 43-52 (1993).

[57] C. He, and J. Zhao, "Modeling rotor wake dynamics with viscous vortex particle method," AIAA J. **47**(4), 902-915 (2009).

[58] J. Zhao, and C. He, "A viscous vortex particle model for rotor wake and interference analysis," J. Am. Helicopter Soc. **55**(1)**,** 12007 (2010).

[59] J. S. Jang, S. H. Park, and D. J. Lee, "Prediction of Fuselage Surface Pressures in Rotor–Fuselage Interactions Using an Integral Solution of Poisson Equation," J. Am. Helicopter Soc. **59**(4)**,** 042001 (2014).

[60] G. S. Winckelmans, and A. Leonard, "Contributions to Vortex Particle Methods for the Computation of Three-Dimensional Incompressible Unsteady Flows," J. Comput. Phys. **109**(2)**,** 247-273 (1993).

[61] S. Y. Wie, D. K. Im, J. H. Kwon, D. J. Lee, K. H. Chung, and S. B. Kim, "Helicopter rotor noise in the merged tip-vortex and blade interaction condition," International Journal of Aeroacoustics **10**(4), 427-442 (2011).

[62] F. Farassat, and G. P. Succi, "The Prediction of Helicopter Rotor Discrete Frequency Noise," Vertica **7**(4), 309-320 (1983).

[63] K. S. Brentner, "Prediction of helicopter rotor discrete frequency noise for three scale models," J. Aircraft, **25**(5), 420-427 (1988).

[64] N. S. Zawodny, D. D. Boyd Jr, and C. L. Burley, "Acoustic Characterization and Prediction of Representative, Small-Scale Rotary-Wing Unmanned Aircraft System Components," in *American Helicopter Society (AHS) 72nd Annual Forum & Technology Display,* 2016.